A Fast-Dynamic Unipolar Switching Control Scheme for Single-Phase Inverters in DC Microgrids

Mandip Pokharel, *Student Member, IEEE*, Nicolai Hildebrandt, *Student Member, IEEE*, Carl Ngai Man Ho, *Senior Member, IEEE*, and Yuanbin He, *Member, IEEE*

***Abstract*—This paper presents the digital implementation of a boundary controller with unipolar switching characteristic for single-phase voltage source full-bridge inverters. This paper expands the application of a second-order switching surface-based control method to unipolar switching of single-phase voltage source inverters (VSIs) using a finite-state machine. The finite-state machine has been formulated considering four different states of the inverter; positive, ZERO1, negative, and ZERO2. The second-order boundary control governs the current state of the system and provides proper switching action to keep the system within the desired reference. The control law is implemented digitally in F28m35x digital control card. A full-bridge inverter topology is used to achieve the three-level voltage switching. Various simulations and experiments were performed in a 550 VA, 120 V, 60 Hz VSI with a digitally implemented controller to verify the theoretical predictions. A high-quality voltage output was obtained for various loading conditions. The transient performance of the controller was investigated using a reference and load changes. A comparison of the implementation was made with the existing classical controllers to verify the fast-dynamic response of the system.**

***Index Terms*—Boundary control, direct current (dc) microgrid, finite-state machine (FSM), second-order switching surface (SSS), unipolar pulsewidth modulation (UP-PWM), voltage source inverter (VSI).**

I. Introduction

VOLTAGE source inverter (VSI) is a well-known topology in terms of its application. VSIs are widely used in industrial electronics such as uninterrupted power supplies and active voltage conditioners [1]–[4]. A typical VSI topology is shown in Fig. 1. In a direct current (dc) microgrid, VSIs basically act as an interface between the dc grid and typical ac loads, such as household appliances [5]. To sum up the application of the

Manuscript received October 27, 2017; revised January 10, 2018; accepted March 13, 2018. Date of publication March 21, 2018; date of current version November 19, 2018. This work was supported by a grant from the NSERC Discovery Grants program, Canada (Sponsor ID: RGPIN-2016-05952). Part of the work described in this paper was presented at the 8th Annual IEEE Energy Conversion Congress and Exposition. Recommended for publication by Associate Editor V. Agarwal. *(Corresponding author: Carl Ngai Man Ho.)*

M. Pokharel and C. N. M. Ho are with the Department of Electrical and Computer Engineering, University of Manitoba, Winnipeg, MB R3T 5V6, Canada (e-mail:

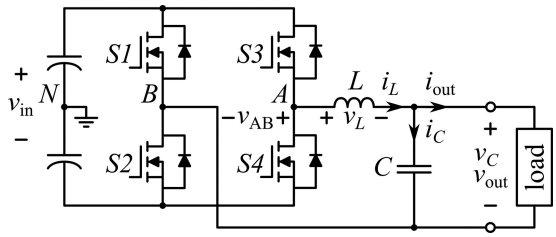

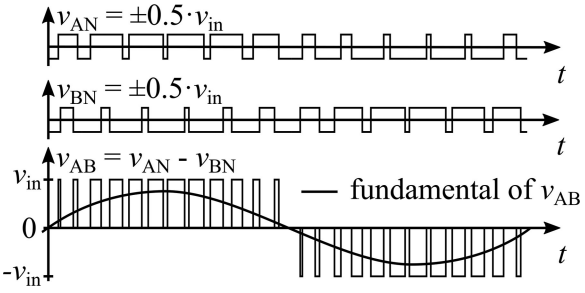

Fig. 2. PWM with unipolar switching.

topology. Basically, the control methodology takes the steady-state characteristics into account in its control law. In order to simplify the control law, two-level (2-L) switching topologies are chosen [8]. It is well known that using the 2-L switching scheme in an FB inverter leads to higher current ripple or larger inductor size and losses compared to a three-level (3-L) switching scheme [14]–[17]. Although a multilevel switching scheme of boundary control with SSS has been proposed by Chan *et al*. [18], it is for general 3-L topologies, for example, neutral point clamped (NPC), T-NPC, and flying-caps topologies. If it is applied to an FB VSI, two semiconductor switches will work at higher switching frequency (e.g., 20 kHz), and other two semiconductor switches will work at line frequency (e.g., 60 Hz), thereby causing the losses to concentrate on the high-frequency switching devices. This leads to higher thermal stress on the devices, thus requiring a larger cooling system. Thermal management is one of the critical design criteria in designing the VSI for dc microgrids applications as it requires higher power density to fit into a very small outlet box to convert a dc voltage to an ac voltage powered loads [19], [20].

This paper proposes the application of boundary control with SSS for the unipolar switching scheme of the FB VSI using a finite-state machine (FSM) method. This allows to extend the application of the unipolar switching scheme to achieve a fast-dynamic response keeping all the switches within their thermal limits. This is as a result of a uniformly distributed switching signal given by the controller. This also helps to bring down the size requirement of passive components. The ideal switching waveforms of unipolar operation are shown in Fig. 2.

The fact that all semiconductor switches switch at the same switching frequency can result in better thermal management of the devices. The proposed controller uses a FSM to determine the converter switching state based on the trajectory selected by the control law implemented in DSP. The control concept has been successfully verified by simulations and experimental results with a 550 VA, 120 V, 60 Hz FB VSI prototype. The results show the system operating with an unipolar switching scheme. The dynamic performance of the controller has been tested during large signal disturbances, such as load step changes and reference voltage changes. To verify the claim of a better dynamic response with the proposed method, a comparison has been made with a traditional proportional-integral (PI)-based controller as well as other controllers like decoupled PI and a nonideal proportional resonant (PR) controller.

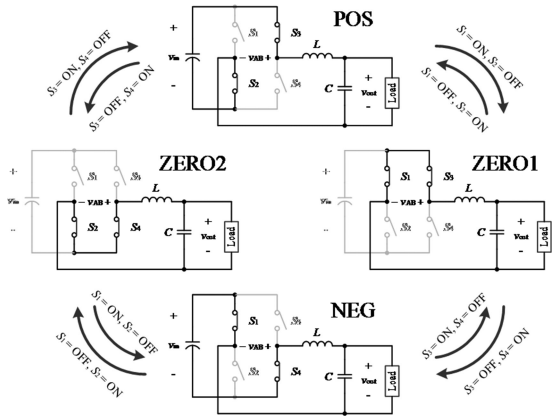

Fig. 3. Unipolar switching states.

TABLE I
INVERTER STATES

Inverter state	$\{\boldsymbol{q}_1;\boldsymbol{q}_2\}$	$\{\boldsymbol{S}_1;\boldsymbol{S}_2;\boldsymbol{S}_3;\boldsymbol{S}_4\}$	$\boldsymbol{v}_{\mathrm{AB}}$	Trajectory family
POS	$\{1;0\}$	$\{\mathrm{OFF};\mathrm{ON};\mathrm{ON};\mathrm{OFF}\}$	v_{in}	Positive
NEG	$\{0;1\}$	$\{\mathrm{ON};\mathrm{OFF};\mathrm{OFF};\mathrm{ON}\}$	$-v_{\mathrm{in}}$	Negative
ZERO1	$\{0;0\}$	$\{\mathrm{ON};\mathrm{OFF};\mathrm{ON};\mathrm{OFF}\}$	0 V	Freewheeling (zero)
ZERO2	$\{1;1\}$	$\{\mathrm{OFF};\mathrm{ON};\mathrm{OFF};\mathrm{ON}\}$	0 V	Freewheeling (zero)

II. PRINCIPLE OF OPERATION

A. Switching Patterns of a Unipolar Switching Control Scheme

A FB VSI topology is shown in Fig. 1. It consists of a dc voltage source, four switches, four antiparallel diodes, a *LC* output filter, and a load connecting to the middle of each arm at the junctions *A* and *B*. By switching v_{AB} between the dc input voltage $+v_{\mathrm{in}}$ and $-v_{\mathrm{in}}$ with switches (S2, S3) ON, (S4, S1) OFF and (S4, S1) ON, (S2, S3) OFF, a bipolar pulsewidth modulation (PWM) is performed [12], [13]. To have unipolar PWM (UP-PWM) as shown in Fig. 2, two more freewheeling switch combinations are needed. The freewheeling switching combinations

$$\{\mathrm{S1};\mathrm{S2};\mathrm{S3};\mathrm{S4}\} = \{\mathrm{ON};\mathrm{OFF};\mathrm{ON};\mathrm{OFF}\} \text{ and}$$
$$\{\mathrm{S1};\mathrm{S2};\mathrm{S3};\mathrm{S4}\} = \{\mathrm{OFF};\mathrm{ON};\mathrm{OFF};\mathrm{ON}\}$$

that yields $v_{\mathrm{AB}} = 0$ V are used in alternation with active switch combinations to achieve UP-PWM.

Fig. 3 shows the equivalent circuits during each switching state of a FB VSI with UP-PWM switching scheme. It can be seen that two switches in an arm are changed at the same time for each state change. Besides, there are two possible zero states, ZERO1 and ZERO2, in the circuit state diagram. Table I presents the summary of the four inverter states. The VSI has same electrical responses in both the zero states but the inductor current is freewheeling with two different paths. The state-space equations for describing the operation of the FB VSI are

$$\dot{x} = A_0 x + B_0 v_{\mathrm{in}} + \sum_{i=1}^{2} (A_i x + B_i v_{\mathrm{in}}) q_i \qquad (1)$$

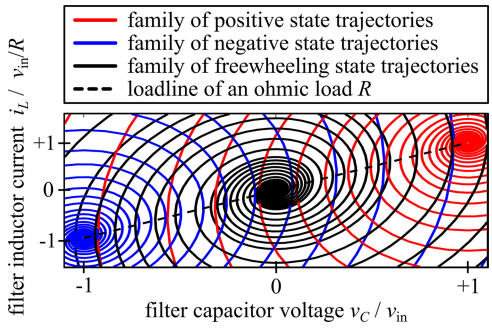

Fig. 4. System trajectories of a full-bridge voltage source inverter.

where $x = \begin{bmatrix} i_L \\ v_C \end{bmatrix}$, $A_0 = \begin{bmatrix} 0 & -1/L \\ 1/C & -1/RC \end{bmatrix}$, $B_1 = \begin{bmatrix} 1/L \\ 0 \end{bmatrix}$, $B_2 = \begin{bmatrix} -1/L \\ 0 \end{bmatrix}$.

Matrices A_1, A_2, and B_0 are empty and $q_i(t)$ are the switching functions of the switched structure system. The system trajectories of system (1) are shown in Fig. 4. Three different families of trajectories defined by following conditions are obtained.

1) When $\{q_1; q_2\} = \{1; 0\}$, the family of positive state trajectories (in red) is active, the system of equations in (1) converges to $[v_C; i_L] = [v_{\text{in}}; v_{\text{in}}/R]$. The corresponding circuit is "POS" in Fig. 3.
2) When $\{q_1; q_2\} = \{0; 1\}$, the family of negative state trajectories (in blue) is active, the system of equations in (1) converges to $[v_C; i_L] = [-v_{\text{in}}; -v_{\text{in}}/R]$. The corresponding circuit is "NEG" in Fig. 3.
3) When $\{q_1; q_2\} = \{1; 1\}$ and $\{0; 0\}$, the family of freewheeling state trajectories (in black) is active, the system of equations in (1) converges to $[v_C; i_L] = [0\text{ V}; 0\text{ A}]$. The corresponding circuits are "ZERO1" and "ZERO2" in Fig. 3.

B. Control Law for the Output Voltage Control With Unipolar Switching Scheme

The system trajectories can be approximated by SSS for all three positive, negative, and the freewheeling states. In this paper, in order to achieve unipolar switching, positive and freewheeling trajectories are used during the positive half-wave of the reference voltage $v_{\text{ref}}(t)$ (mode I), and negative and freewheeling trajectories are used during the negative half-wave of $v_{\text{ref}}(t)$ (mode II). Fig. 5 shows the ideal trajectories during mode I and mode II operations.

Four different switching criteria, two for each modes, can be determined based on switching instants dictated by the boundary control law using a similar approach as in [3], [4], [8], and [10]–[13].

The switching criterion for taking a positive trajectory, i.e., applying $+v_{\text{in}}$ to the terminal *A–B* of the *LC* filter during mode I is

$$v_C(t) \le v_{C,\min}(t) + k_1(v_{\text{in}}, v_{\text{ref}}) \cdot i_C^2(t) \quad \text{and} \quad i_C(t) < 0 \tag{2}$$

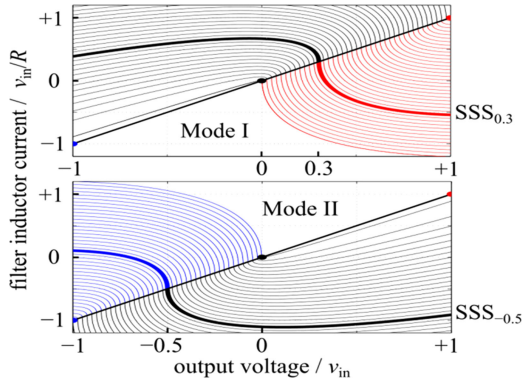

Fig. 5. Unipolar second-order switching surfaces (SSS) for positive (mode I) and negative (mode II) reference voltage.

where $v_{C,\min}$ is the lower boundary of the voltage hysteresis and the parameter k_1 given as the function of v_{in} and v_{ref} is represented by (6). *L* and *C* are the nominal values of the *LC* filter.

The switching criterion for taking a freewheeling trajectory, i.e., applying 0 V to the terminal *A–B* of the *LC* filter during mode I is

$$v_C(t) \ge v_{C,\max}(t) - k_2(v_{\text{ref}}) \cdot i_C^2(t) \quad \text{and} \quad i_C(t) > 0 \tag{3}$$

where $v_{C,\max}$ is the upper boundary of the voltage hysteresis and k_2 given as the function of v_{ref} is represented by (7).

Similarly, in mode II where v_{ref} is negative, the switching criterion for taking a negative trajectory is

$$v_C(t) \ge v_{C,\max}(t) - k_3(v_{\text{in}}, v_{\text{ref}}) \cdot i_C^2(t) \quad \text{and} \quad i_C(t) > 0 \tag{4}$$

with k_3 given as the function of v_{in} and v_{ref} represented by (8).

The switching criterion for taking a freewheeling trajectory in mode II is

$$v_C(t) \le v_{C,\min}(t) - k_2(v_{\text{ref}}) \cdot i_C^2(t) \quad \text{and} \quad i_C(t) < 0 \tag{5}$$

$$k_1(v_{\text{in}}, v_{\text{ref}}) = \frac{L}{2C} \frac{1}{v_{\text{in}}(t) - v_{\text{ref}}(t)} \tag{6}$$

$$k_2(v_{\text{ref}}) = \frac{L}{2C} \frac{1}{v_{\text{ref}}(t)} \tag{7}$$

$$k_3(v_{\text{in}}, v_{\text{ref}}) = \frac{L}{2C} \frac{1}{v_{\text{in}}(t) + v_{\text{ref}}(t)}. \tag{8}$$

A detailed derivation of (2)–(8) is presented in the Appendix.

Switching surfaces for mode I and mode II are illustrated in Fig. 5. Switching boundaries when $v_{\text{ref}} = 0.3 \cdot v_{\text{in}}$ and $v_{\text{ref}} = -0.5 \cdot v_{\text{in}}$ are highlighted; the switching hysteresis $v_{\max} - v_{\min}$ is neglected. The surfaces represented by Fig. 5 are very close to the ideal trajectories shown in Fig. 4. The typical steady-state waveforms during mode I and model II operations are shown in Fig. 6.

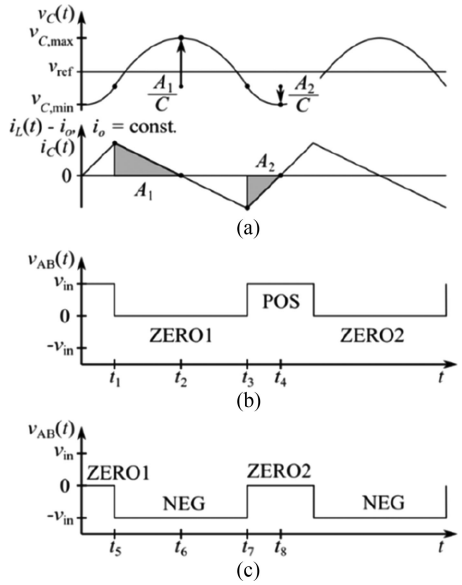

Fig. 6. Typical waveforms in steady-state operation and corresponding inverter states in mode I and mode II.

III. Steady-State Characteristics

A. Duty Ratio

The duty ratio of an inverter would be a time-varying quantity dependent on the position of the output voltage magnitude varying as a sinusoidal quantity. At the same time, the operating principle of an inverter may be compared to that of a buck converter and the relation of a duty cycle can be easily derived.

The output voltage of the inverter can be expressed taking into assumption the steady-state output voltage equal to the reference voltage as follows:

$$v_C(t) = v_{\text{ref}}(t) = V_m \sin\omega t \tag{9}$$

where V_m is the peak value of the output sinusoidal voltage.

Taking into account the fact that source voltage of the *LC* filter across terminal *AB* is changing between positive voltage and zero voltage when the inverter output voltage is in the positive half cycle, the following relation can be obtained:

$$D(t) = \frac{V_m \sin\omega t}{V_{\text{in}}} \tag{10}$$

where V_{in} is the input dc voltage.

B. Inductor Current Ripple

The inductor current ripple may be expressed in the similar method implied by the buck converter steady-state equations. Taking turn ON condition in the positive half cycle where the inductor current increases

$$\frac{dI_L}{dt} = \frac{V_{\text{in}} - V_m \sin\omega t}{L} \Rightarrow \Delta I_L(t) = \left(\frac{V_{\text{in}} - V_m \sin\omega t}{L}\right)\frac{D(t)}{f_{\text{sw}}}. \tag{11}$$

This shows the inductor current ripple is also varying along with the duty ratio if the switching frequency is assumed constant. The above-mentioned equation may further be expanded as

$$\Delta I_L(t) = \frac{(V_{\text{in}} - V_m \sin\omega t)\, V_m \sin\omega t}{L f_{\text{sw}} V_{\text{in}}}. \tag{12}$$

C. Capacitor Voltage Ripple

The capacitor voltage ripple is controlled by boundary control defined by the hysteresis band Δ.

The capacitor voltage ripple is basically a contribution of the inductor current ripple assumed equivalent to the capacitor current. Hence, the steady-state equation for capacitor voltage can be expressed as

$$\Delta V_c(t) = \frac{\Delta I_L(t)}{8C f_{\text{sw}}} = \frac{(V_{\text{in}} - V_m \sin\omega t)\, V_m \sin\omega t}{8LC f_{\text{sw}}^2 V_{\text{in}}}. \tag{13}$$

D. Switching Frequency

The equations for inductor current ripple and capacitor voltage ripple have reciprocate relation to the switching frequency. Therefore, if one is fixed, the other varies with time. This way it is difficult to have the measure of switching frequency if the control objective is to maintain the voltage or current ripple.

A relation between the voltage band and switching frequency has been described by [10]. The expression can be rewritten as follows:

$$f_{\text{sw}}(t) = HK\Delta^{-0.5} \tag{14}$$

where

$$H = \frac{(V_{\text{in}} - V_m \sin\omega t)\, V_m \sin\omega t}{L V_{\text{in}}}$$

and

$$K = \frac{\sqrt{k_1 k_2}}{\sqrt{2D(t)\, k_2} + \sqrt{2(1 - D(t))\, k_1}}.$$

The above-mentioned equations are valid for the positive half cycle of the inverter. Similar equations can be derived for the negative half cycle when the inductor source voltage is switching between negative v_{in} and 0. The only change would be in the variables *H* and *K*, which can be expressed as follows:

$$H = \frac{V_m \sin\omega t\,(V_{\text{in}} + V_m \sin\omega t)}{L V_{\text{in}}}$$

$$K = -\frac{\sqrt{k_2 k_3}}{\sqrt{2\left(\frac{1}{D(t)} - D(t)\right) k_2} + \sqrt{2\left(\frac{1}{D(t)} - D(t) - 1\right) k_3}}.$$

Hence, the measure of average switching frequency can be estimated even if the voltage band is fixed.

IV. Controller Design and Implementation

The control law has been implemented using the Texas Instruments F28M35H52C DSP. Fig. 7 shows the block diagram of the designed controller. Three functional blocks are included, analog-to-digital converter, digital control algorithm, and FSM. Source voltage (v_{in}), filter capacitor current (i_C), reference voltage (v_{ref}), and capacitor voltage (v_C) are sampled at 300 kHz. Alternatively, an internally programmed voltage reference is

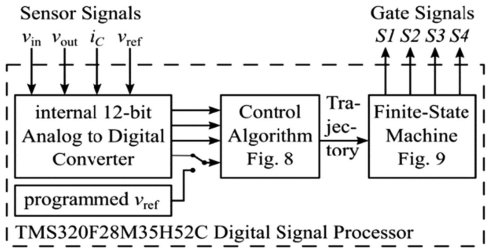

Fig. 7. Structure of the digital inverter control.

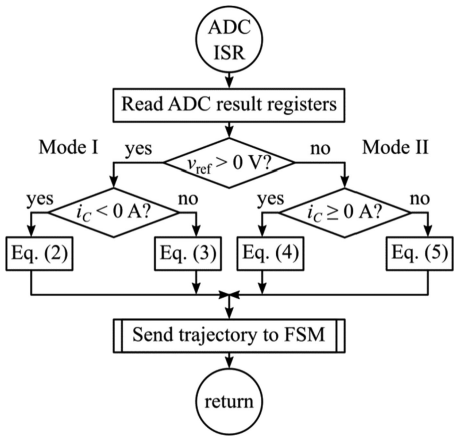

Fig. 8. Digital control algorithm.

used to generate a simple sinusoidal waveform. Subsequently, the digital values are evaluated in the digital control algorithm, the flowchart is shown in Fig. 8. The algorithm determines the switching criteria, which decides the upcoming switching action based on the instantaneous values of the sensed signals. The algorithm comprises two switching criteria each for mode I and mode II. Every interrupt service routine call is followed by the evaluation of one switching criterion. The output of the control algorithm is finally the decision based on the trajectory to be taken; positive (coded "+1"), negative (coded "–1"), or freewheeling (coded "0").

Boundary control laws like SSS have no memory as their actions are based on instantaneous values only [10]. This allows easy implementation of such controllers either analog or digital. To have a uniform distribution of switching losses among all switches, the controller should keep track of previously used switch combination of the freewheeling state. Based on the previous freewheeling switching state, a decision is made by the controller to take alternative switch combination in the current state. The paper proposes a way to use the FSM method to add this memory function without losing the inherent dynamics of the SSS control law.

Fig. 9 shows the state diagram in the FSM, which processes the trajectory decision of the controller to generate necessary gate control signals. The output of each state is listed in Table I. The output of the ZERO1 state is complementary to the output of the state ZERO2. The output of both POS states are identical, evenly the output of both NEG states are identical. As long as the output from the control algorithm does not change, the FSM stays in the same state. So is the gate control signal generated

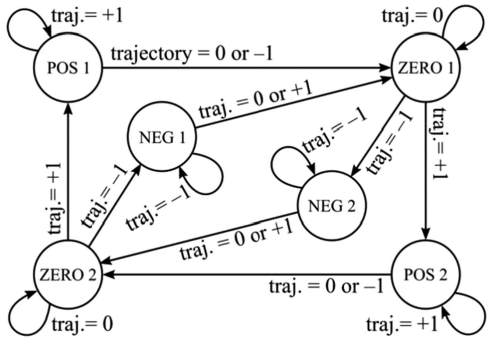

Fig. 9. Unipolar switching finite-state machine.

by the FSM. When a new criterion is satisfied, the FSM changes both its state and output according to the trajectory decision. Taking for instance, during mode I, i.e., positive half of the reference voltage, the FSM circles among states of the "outer circle," i.e., POS1-ZERO1-POS2-ZERO2-POS1. The doubled number of active states, POS1 and POS2, ensures a sequence in which the two freewheeling states ZERO1 and ZERO2 always alternate. This continues until a new criterion is satisfied and the trajectory decision forces a state to switch to the negative state from a previous freewheeling zero state. This occurs when a zero crossing of the reference voltage is encountered and the state after this point circles through the "inner circle" of the FSM. NEG1 and NEG2 in the FSM ensure the alternation of the two freewheeling states.

V. Simulation and Experimental Results

A. Simulation Results—Boundary Controller

The performance and switching patterns of the proposed controller have been verified through various simulations. Fig. 10(a) shows a simulation waveform of an inverter using the proposed controller operating under a sudden load change condition. The load change is made from 97 to 57 Ω and vice versa. It is seen that the output voltage remains a pure sinusoid before and after the load transients. Also from the waveform, it can be inferred that the voltage can return to the steady state in two switching actions after the load transient. The system is throughout operating with the UP-PWM scheme as shown in the simulated waveforms in Fig. 10(a). Fig. 10(b) further shows an *X–Y* chart of the waveforms between inductor current and capacitor voltage. It illustrates that the inverter is initially operating in mode I and is therefore operating with a positive trajectory around a 97 Ω load line. The system trajectory runs through a freewheeling state to a negative trajectory (mode II), where at the peak of the voltage, it encounters a large load transient of 57 Ω. The controller immediately responds to this transient and starts following a new load line. The new steady-state operating point is reached within two switching actions. Similar action is seen when the load transient (57–97 Ω) occurs at the peak of the positive half cycle.

Fig. 11(a) and (b) shows simulation waveforms and phase plane plot of an inverter using the proposed controller operating under reference voltage transients. The reference voltage is

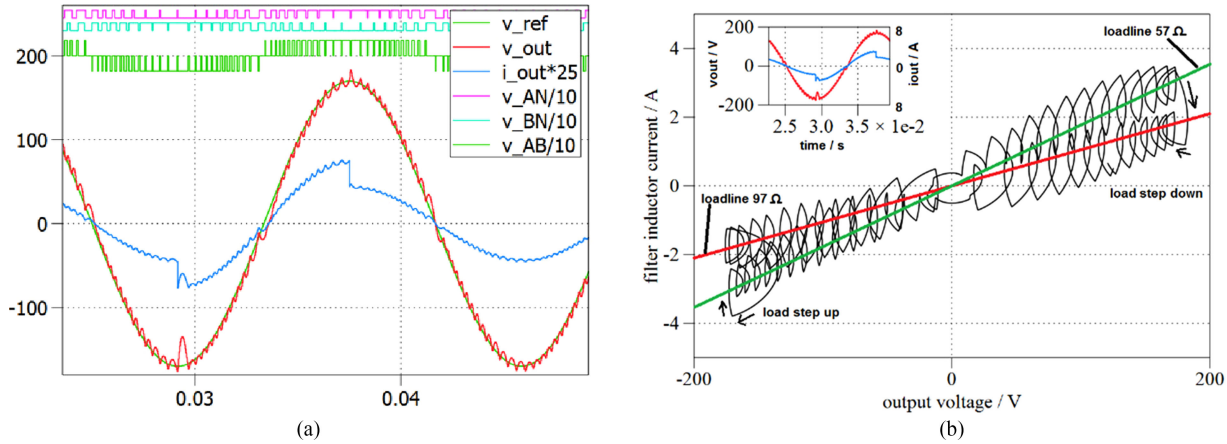

Fig. 10. Simulated results of load change transient from 97 to 57 Ω and vice versa. (a) Time domain. (b) Phase plane.

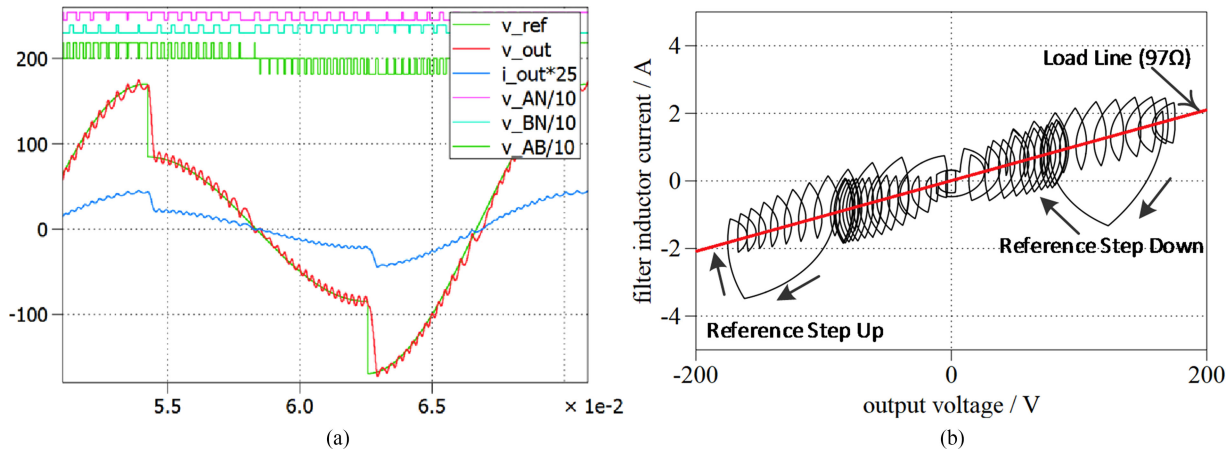

Fig. 11. Simulated results of reference voltage change transient from 120 to 60 V and vice versa; with 97 Ω load. (a) Time domain. (b) Phase plane.

changed from 120 to 60 Vrms and back to 120 Vrms. Similar observations to the case of load transients can be made. The output voltage immediately follows the reference voltage step change. The system is throughout operating with the UP-PWM scheme. The new operating point is again reached within two switching actions.

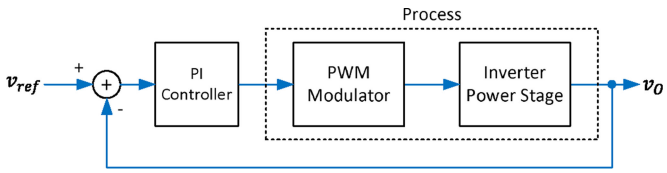

Fig. 12. Inverter control with directly implemented PI.

B. Simulation Results—PI and PR Controller

To have a reference to validate the fast-dynamic performance of a boundary control based VSI, three simulation cases were made; one with a conventional PI controller, second with a reference frame PI, and the final one with a PR controller.

1) Directly Implemented PI Controller: The simplified block diagram of a directly implemented PI controller is shown in Fig. 12. The controller parameters are chosen using frequency response plots. The inverter power stage is modeled using a state-space averaging technique. Using the designed parameters, the steady-state and transient performance of the controller is studied.

2) PI Controller Implemented With Reference Frame Transition: The PI controller in Fig. 12 can be transformed into a d–q reference frame by creating two orthogonal sinewaves. A transport delay of one quarter is used to create an orthogonal vector of the reference sinewave, which is then converted to a d–q axis frame using α–β to d–q transformation. Similar approach is followed for the output sinewave. The reference d-axis, q-axis voltages, and measured d-axis, q-axis voltages are fed to individual PI controllers. Since d and q-axes are dc values, the use of the PI controller on individual voltages would result in a zero steady-state error [22]. The simulation case of a decoupled PI controller is made to study the steady-state and transient performance of the controller.

3) PR Controller: In terms of achieving the zero steady-state error, the PR controller acts the same way as a decoupled PI controller. A nonideal PR controller is chosen for comparison due to its lower sensitivity variation to resonance frequency drift. The

TABLE II
CONTROLLER PARAMETER COMPARISON

Parameters	Controller type			
	PI	Decoupled PI	PR	Boundary
Steady-state error (%)	0.58	0.0431	0.071	Always within the boundary specified
% Peak overshoot	88.03	72.89	91.67	
Settling time (2%)	2.82 ms	2.2 ms	2.06 ms	296 μs

TABLE III
SPECIFICATION OF THE PROTOTYPE

Parameter	Value	Parameter	Value
Input voltage V_{in}	185 V	Output filter inductance L	7 mH
Output voltage V_{out}	120 V	Output filter capacitance C	4.7 μF
Rated power P_O	550 VA	Switching frequency $f_{\text{sw,avg}}$	4 kHz

transfer function of the nonideal PR controller is represented by

$$G_{\text{pr}}(s) = K_p + \frac{2K_i\omega_c s}{s^2 + 2\omega_c s + \omega_o} \tag{15}$$

where K_p is the proportional gain, K_i is the integral gain, ω_o is the resonant frequency, and ω_c is the cutoff frequency [23]. A simulation was made to study the performance of this controller with the inverter.

It is clearly seen from Table II that application of boundary control for a single-phase FB VSI with unipolar switching can result in a better transient tracking performance at the same time having flexibility over other controller parameters.

C. Experimental Results—Steady-State Operation

A 550 VA, 185 V input dc voltage and 120 Vrms output ac voltage FB VSI prototype was used to verify the proposed controller under the unipolar switching scheme with boundary control law implemented through a digital control under different loading conditions. Table III shows the specification and critical component parameters of the system.

Fig. 13 shows the steady-state waveforms of the prototyped VSI working with different loadings. In the diagrams, channel 1 shows the capacitor voltage; channel 2 represents the voltage across the midpoints of two arms (V_{AB}); channel 3 represents the switching instant of the lower arm switch of branch A; and channel 4 represents the output load current.

Fig. 13(a) shows waveforms when the system is working under no-load condition. The output voltage shows a purely sinusoidal voltage. The voltage across two arms (V_{AB}) shows that the system is in unipolar operating mode and the switching instant of the lower arm switch shows that the switching is working in high frequency at all times. Fig. 13(b) shows waveforms when the system is working with a 57 Ω resistor (250 W). The output voltage is still sinusoidal while working in unipolar switching mode. The switching condition is unchanged from that of no-load condition. Fig. 13(c) shows waveforms when the system is working with an inductive load. The load is formed by an inductor and a resistor bank. It draws 550 VA power, and the measured power factor of the load is 0.78. The output volt-

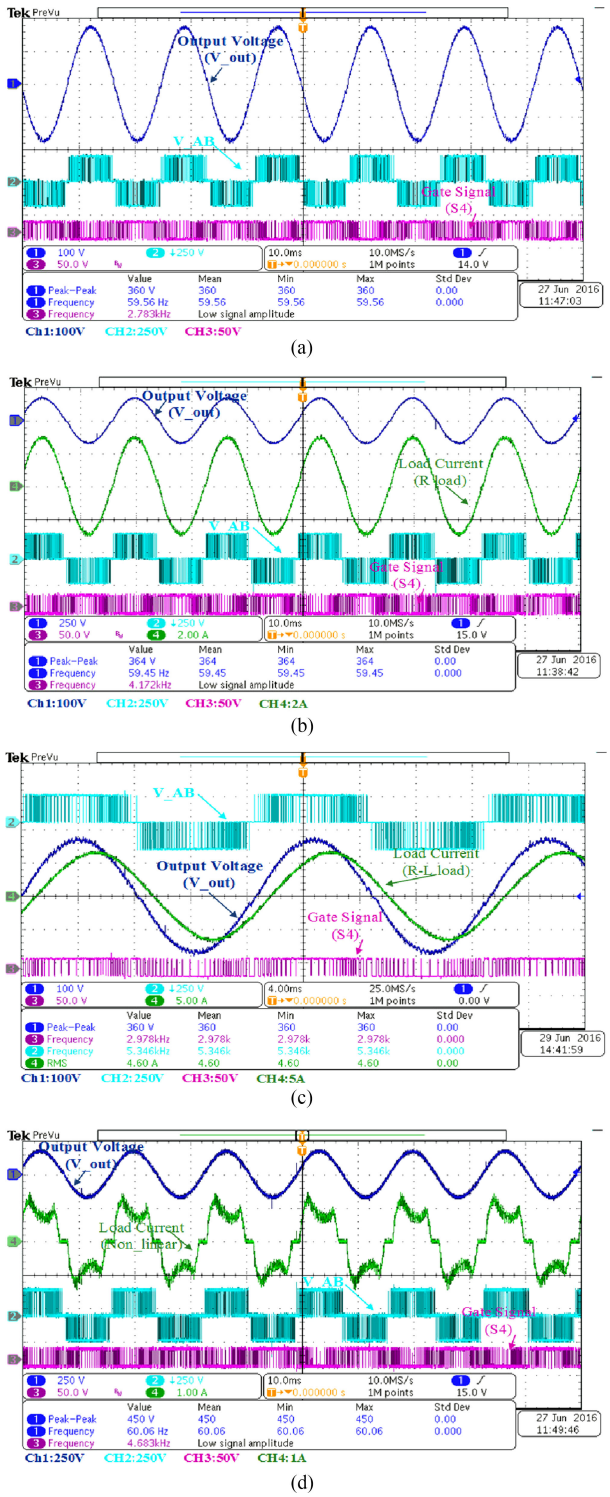

Fig. 13. Experimental results in steady-state operation. (a) No-load condition. (b) 250 W linear load. (c) 550 VA inductive load. (d) 100 W nonlinear loads.

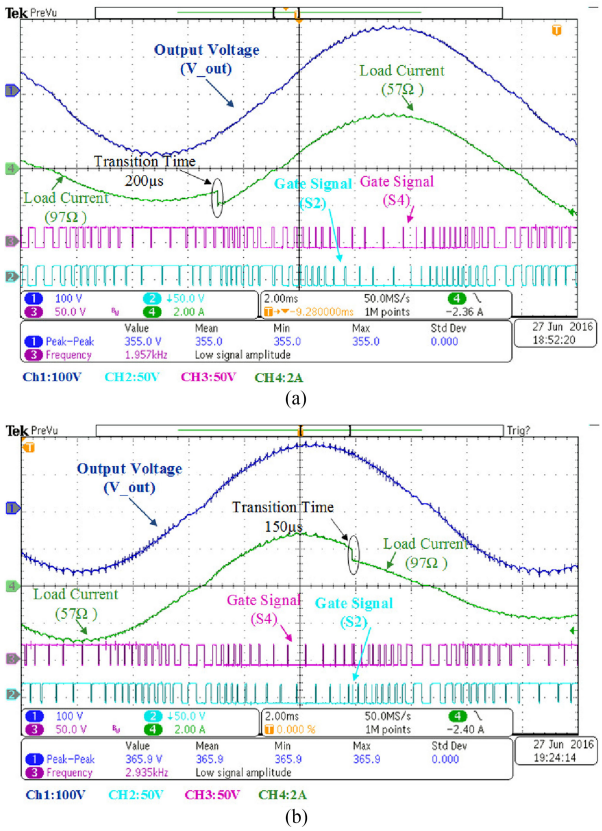

Fig. 14. Experimental results in load step change transient. (a) 97–57 Ω. (b) 57–97 Ω.

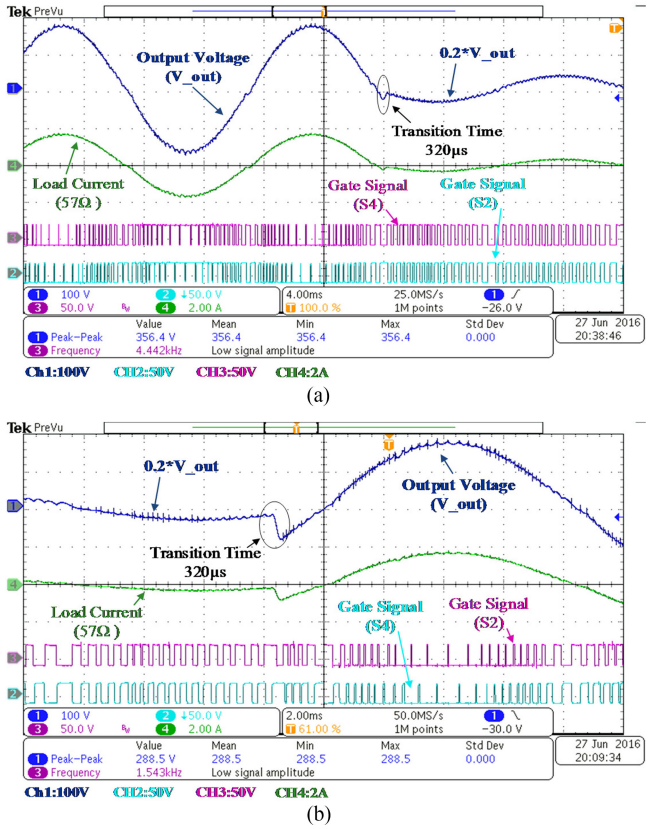

Fig. 15. Experimental validation of the controller for change in reference by 80% from 120 V (rms) to 24 V (rms) and back to 120 V (rms).

age is a purely sinusoidal wave maintaining unipolar switching operation.

In order to verify the VSI working with a dc microgrid, nine commercial 12 W LED light bulbs were connected to the output of the VSI. It was to replicate a conventional lighting network connected to a dc microgrid. Moreover, the front stage of the LED light bulbs is a diode bridge, and this is used to test the controller performance under nonlinear load characteristics. The waveforms are shown in Fig. 13(d). It shows that the output voltage is kept sinusoidal and without distortion.

The measured voltage total harmonic distortions (THD) in all steady-state operations are in the range of 1.27–1.5%. This signifies that the VSI provides a high-quality output voltage under all loading conditions, at the same time remaining well below the limit specified by the international standard IEEE 519 [21]. The experimental results verified that the VSI with the proposed controller can operate to provide a high-quality sinusoidal voltage independent of the loading conditions. The sustained voltage output avoids any interference with the loads, which would generate harmonic and subsequently contribute to higher losses in the loads.

D. Experimental Results—Load Step Change Transient

The controller operation for the load step is demonstrated through experimental results presented in Fig. 14, which shows a step change of load from 97 to 57 Ω (150–250 W) and back to 97 Ω (250–150 W). The experimental result shows proper agreement with the theoretical predictions and simulation. The change in load step seeks for new operating point, which has to be determined by the controller. The experimental results show a fast-dynamic performance of the controller to reach a new stable operating point for a load step change. The results show that transients have no effect on the quality of output voltage waveform. The gate signals in Fig. 14 show that the system works with unipolar switching, which is the same as the typical waveform in Fig. 2. The time for the controller to find a new operating point after the transient is recorded is 150–200 μs.

E. Experimental Results—Reference Voltage Step Change Transient

To have a better understanding of operation and performance of the controller, controller response to a change in reference voltage can further be analyzed. Fig. 15 shows waveforms when the output voltage reference changes from 120 to 24 V with a 97 Ω linear load. Although it may not happen in an ac grid emulator for dc microgrids, it is important to evaluate the dynamic performance of the proposed controller under all conditions.

The waveform of the output voltage (channel 1) in Fig. 15 follows the reference voltage change. It is to be noted that, as the reference has been generated through the DSP, this change in the reference is made internally. The load current (channel 4) exactly follows the load voltage. The important thing here to be noticed is the performance of the controller even in the case of a huge step change of 80%. The controller finds the

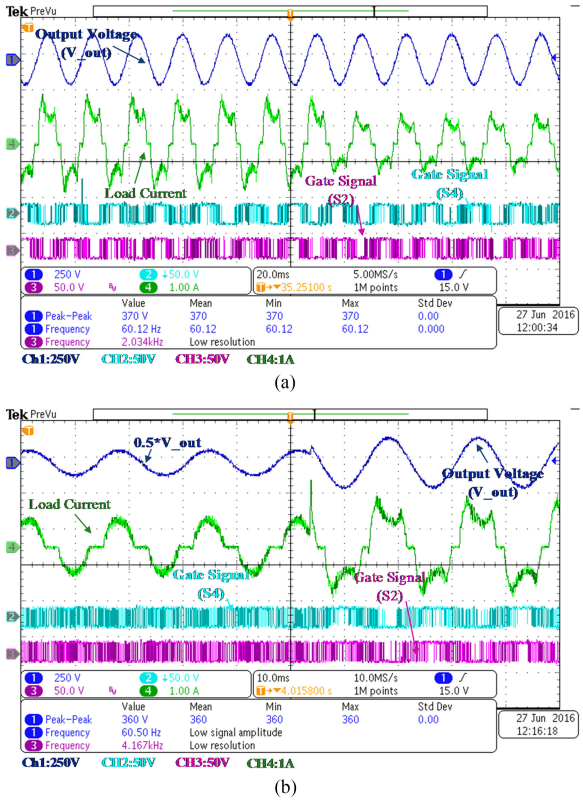

Fig. 16. Dynamic performance of the controller under nonlinear loading conditions. (a) Load change. (b) Reference change.

stable operating point within two switching actions and forcing the output voltage to reach the desired value. This has been studied for both the cases of increasing and decreasing reference steps. The output voltage keeps sinusoidal, without distortion and stable before and after the transients.

The time taken by the system from the instant of reference change to finding a next steady-state operating point is recorded to be 320 μs. This is the time taken by the controller to find a new stable operating point. This is almost ten times smaller compared to results from the conventional PI-based controller scheme shown in Section V-F, which has its transition time in the range of few milliseconds. This can be a good standing point for stating the tight performance of the controller even under severe transient conditions. This has also been verified through simulation results in Section V-B, where the various controller parameters are analyzed under reference transients.

F. Experimental Results—Transients With Nonlinear Loads

To further demonstrate the performance of the controller, various tests were carried out even under nonlinear loading conditions. For the sake of realization of nonlinear load, nine 12 W LED lamps were connected in parallel with the provision of switching a group of three lamps each with one respective switch.

To study the transient performance of the controller due to nonlinear loading step, one switch was turned ON and OFF during different times and the result was recorded. Similarly, the controller performance was recorded for change in reference

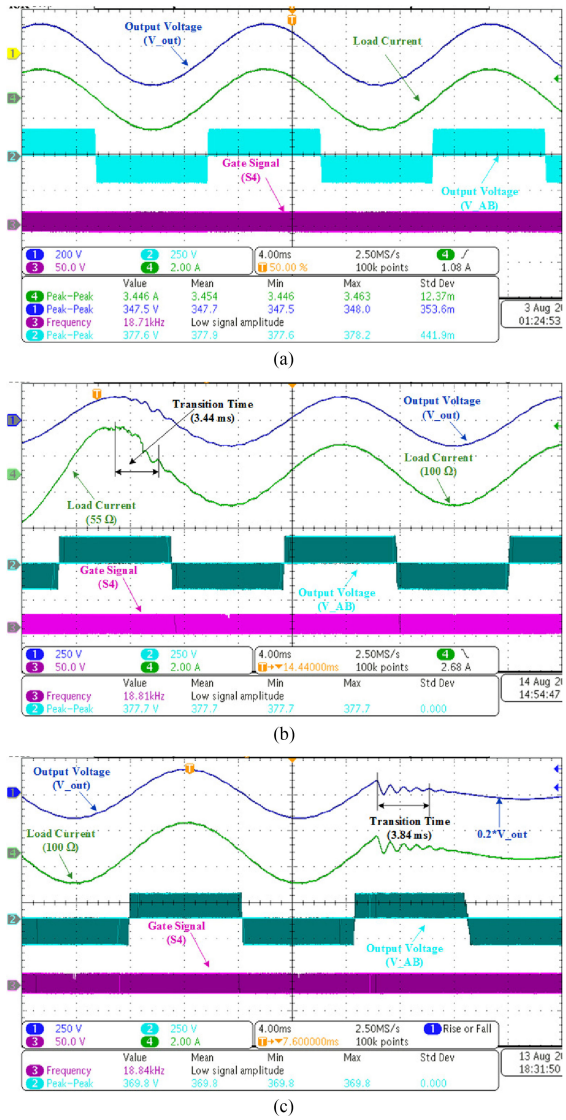

Fig. 17. Performance of the PI controller. (a) Steady state. (b) Load change. (c) Reference change.

steps. Fig. 16(a) shows the response of the controller for a step change in load and reference voltage. For the step change in load, the output is changed to the next corresponding stable operating point in a very short time. Similarly, for the case of change in the reference voltage in Fig. 16(b), the output voltage tracks the reference voltage immediately. Two switching actions are enough for the controller to reach to the next steady-state operating stable point. Since the inverter is used in dc microgrids, potentially dimmer function can be integrated into the inverter by changing the output voltage reference. Fig. 16(b) shows that the output voltage has a sudden change from 60 to 120 V. The VSI reacts very fast without affecting the quality of the output voltage before and after the transient.

G. Experimental Results—Conventional PI-Based Controller

A unipolar FB VSI with a conventional PI-based controller has been simulated and accordingly implemented through a DSP as a benchmark case. Steady-state and transient performance of

TABLE IV
TABLE OF MEASUREMENTS

Calculated	Measured			
P.f.	P.f.		THD (%)	Efficiency (%)
0.9727	0.9739	Leading	1.8830	95.95
0.9025	0.9072		1.8505	95.84
0.7234	0.7288		1.6371	95.36
0.5727	0.5829		1.4405	95.04
1	1	Unity	1.7025	97.75
1	1		1.9550	95.78
0.9651	0.9442	Lagging	1.6368	96.07
0.9888	0.9809		1.4750	97.58
0.8671	0.882		1.2407	98.38
0.6954	0.7373		1.4680	96.59

the controller has been investigated under various operating scenarios. The steady-state operation of the system shows the output voltage in track with the reference voltage. The stable performance of the system under both steady and transient conditions is shown in Fig. 17. The dynamic performance of the system during load and reference change shows a transition time of 3.44 ms [see Fig. 17(b)] and 3.84 ms [see Fig. 17(c)], respectively.

H. Performance Analysis of the Controller

The dynamic performance of the proposed scheme has been demonstrated from Sections V-A–V-F. Furthermore, to analyze the performance of the system, THD and efficiency of the system were recorded under various loading conditions.

The efficiency of the system under leading, lagging, and unity power factor conditions shows measurements above 95%, Table IV. Similarly, THD measurements under leading, lagging, and unity power factor are recorded as shown in Table IV. The THD measurements are well under 5% under all loading conditions. These measurements show the high-quality performance of the proposed controller.

VI. CONCLUSION

This paper presented a fast-dynamic response and unipolar switching control scheme for single-phase VSIs, particularly for interfacing a dc microgrid and ac loads. The control technique allowed the output voltage of the VSI to achieve a steady-state value very fast as compared to a traditional controller after the disturbance. In addition, it gave a 3-L switching voltage waveform at the output with an uniform switching frequency in all four semiconductor switches. This allows to have semiconductor losses distributed equally among all four switches. The controller implemented provided a proper control signal to follow the right SSS based on the reference voltage change or load step change. The FSM was used to provide the proper switching instants to implement the unipolar switching of the VSI. The mathematical models were provided and explained. A prototype of unipolar switching FB inverter was built and the control scheme was implemented in a DSP. The control scheme was successfully verified through computer simulations and experimental results. Simulations and experimental results all showed a good agreement with the theory.

APPENDIX

A. Derivation of the Switching Criteria for Mode I and Mode II

In mode I, i.e., for $v_{\rm ref} > 0$ V, the criteria derivations largely correspond to those for the buck converter, as shown in Fig. 1. The criteria are derived for steady-state waveforms shown in Fig. 6.

Assuming the average capacitor voltage $\overline{v_C}$, which is identical to the average output voltage $\overline{v_{\rm out}}$, to be equal to the reference voltage $v_{\rm ref}$ during the considered time intervals, the voltage across the inductor *L* is

$$v_L = \begin{cases} -\overline{v_C} = -v_{\rm ref} & \text{for } t = [t_1; t_2] \\ v_{\rm in} - \overline{v_C} = +v_{\rm in} - v_{\rm ref} & \text{for } t = [t_3; t_4] \\ -v_{\rm in} - \overline{v_C} = -(v_{\rm in} + v_{\rm ref}) & \text{for } t = [t_5; t_6] \\ -\overline{v_C} = -v_{\rm ref} & \text{for } t = [t_7; t_8] \end{cases} \tag{A.1}$$

$$v_L = L\frac{di_L}{dt}$$
$$i_C = C\frac{dv_C}{dt}$$
$$dv_C = \frac{1}{C} i_C\, dt. \tag{A.2}$$

By applying Kirchhoff's current law for the capacitor current and assuming the output current $i_{\rm out}$ to be constant during the time intervals of interest, we get

$$\frac{di_C}{dt} \cong \frac{di_L}{dt} = \frac{v_L}{L}$$
$$dt = \frac{L}{v_L} di_C. \tag{A.3}$$

Putting (A.3) into (A.2) integrated over $[t_a; t_b]$ yields

$$\begin{aligned} v_C\,(t_b) - v_C\,(t_a) &= \int_{t_a}^{t_b} dv_C = \frac{1}{C}\int_{t_a}^{t_b} i_C\, dt \\ &= \frac{1}{C}\int_{i_C\,(t_a)}^{i_C\,(t_b)} i_C \cdot \frac{L}{v_L} di_C \\ &= \frac{1}{C}\frac{L}{v_L}\frac{1}{2}\left[i_c^2\,(t_b) - i_C^2\,(t_a)\right] = \frac{1}{C} A_{|[t_a;t_b]}. \end{aligned} \tag{A.4}$$

As shown in Fig. 6

$$\begin{aligned} v_C\,(t_2) - v_C\,(t_1) &= A_{|[t1;t2]}/C, \\ v_C\,(t_6) - v_C\,(t_5) &= A_{|[t5;t6]}/C, \\ v_C\,(t_4) - v_C\,(t_3) &= A_{|[t3;t4]}/C \end{aligned}$$

and

$$v_C\,(t_8) - v_C\,(t_7) = A_{|[t7;t8]}/C.$$

In mode I, $v_{\rm AB}(t)$ has to be switched from $v_{\rm in}$ to 0 V at the instant t_1 so that v_C reaches the upper voltage hysteresis

boundary $v_{C,\max}$ at the instant t_2, because the capacitor C will continue being charged with $i_C > 0$ A from the inductor during the freewheeling state after the switching action:

$$v_C\left(t_2\right) = v_C\left(t_1\right) + A_{|[t1;t2]}/C \geq v_{C,\max}$$

with $t_a = t_1,\ t_b = t_2,\ i_C(t_2) = 0$ A and $v_L = -v_{\text{ref}}$ in (A.4) to calculate $A_1 = A_{|[t1;t2]}$, we get

$$v_C\left(t_1\right) \geq v_{C,\max} - \frac{L}{2C}\frac{-i_C^2\left(t_1\right)}{-v_{\text{ref}}}. \tag{A.5}$$

Equation (3) is obtained, which is based on (A.5).

Same upper limit and area displayed as A_1 applies for the switching to $v_{\text{AB}}(t_5) = -v_{\text{in}}$. With $t_a = t_5,\ t_b = t_6,\ i_C(t_6) = 0$ A, and $v_L = -(v_{\text{in}} + v_{\text{ref}})$ in (A.4) to calculate $A_1 = A_{|[t5;t6]}$, we get

$$v_C\left(t_5\right) \geq v_{C,\max} - \frac{L}{2C}\frac{-i_C^2\left(t_5\right)}{-\left(v_{\text{in}} + v_{\text{ref}}\right)}. \tag{A.6}$$

Equation (4) is obtained, which is based on (A.6).

At the instants t_3 and t_7, the capacitor current is negative and a switch action must be taken as soon as the condition is given that the capacitor voltage will go below $v_{C,\min}$, i.e., the equations to be fulfilled are

$$v_{C,\min} \geq v_C\left(t_4\right) = v_C\left(t_3\right) + A_{|[t3;t4]}/C$$

and

$$v_{C,\min} \geq v_C\left(t_8\right) = v_C\left(t_7\right) + A_{|[t7;t8]}/C.$$

With $t_a = t_3,\ t_b = t_4,\ i_C(t_4) = 0$ A, and $v_L = v_{\text{in}} - v_{\text{ref}}$ in the first equation and $t_a = t_7,\ t_b = t_8,\ i_C(t_8) = 0$ A, and $v_L = -v_{\text{ref}}$ in the second equation, we get

$$v_C\left(t_3\right) \leq v_{C,\min} - \frac{L}{2C}\frac{-i_C^2\left(t_3\right)}{v_{\text{in}} - v_{\text{ref}}}. \tag{A.7}$$

Equation (2) is obtained, which is based on (A.7)

$$v_C\left(t_7\right) \leq v_{C,\min} - \frac{L}{2C}\frac{-i_C^2\left(t_7\right)}{-v_{\text{ref}}}. \tag{A.8}$$

Equation (5) is obtained, which is based on (A.8).

REFERENCES

[1] J. M. Guerrero, L. Hang, and J. Uceda, "Control of distributed uninterruptible power supply systems," *IEEE Trans. Ind. Electron.*, vol. 55, no. 8, pp. 2845–2859, Aug. 2008.

[2] P. K. Jain, J. R. Espinoza, and H. Jin, "Performance of a single-stage UPS system for single-phase trapezoidal-shaped ac-voltage supplies," *IEEE Trans. Power Electron.*, vol. 13, no. 5, pp. 912–923, Sep. 1998.

[3] C. Ho, H. Chung, and K. Au, "Design and implementation of a fast dynamic control scheme for capacitor-supported dynamic voltage restorers," *IEEE Trans. Power Electron.*, vol. 23, no. 1, pp. 237–251, Jan. 2008.

[4] C. Ho and H. Chung, "Implementation and performance evaluation of a fast dynamic control scheme for capacitor-supported interline DVR," *IEEE Trans. Power Electron.*, vol. 25, no. 8, pp. 1975–1988, Aug. 2010.

[5] H. Kakigano, Y. Miura, and T. Ise, "Low-voltage bipolar-type dc microgrid for super high quality distribution," *IEEE Trans. Power Electron.*, vol. 25, no. 12, pp. 3066–3075, Dec. 2010.

[6] Y. Tzou and S. Jung, "Full control of a PWM dc-ac converter for ac voltage regulation," *IEEE Trans. Aerosp. Electron. Syst.*, vol. 34, no. 4, pp. 1218–1226, Oct 1998.

[7] A. Abrishamifar, A. Ahmad, and M. Mohamadian, "Fixed switching frequency sliding mode control for single-phase unipolar inverters," *IEEE Trans. Power Electron.*, vol. 27, no. 5, pp. 2507–2514, May 2012.

[8] K. Au, C. Ho, H. Chung, W. H. Lau, and W. T. Yan, "Digital implementation of boundary control with second-order switching surface for inverters," in *Proc. IEEE Power Electron. Spec. Conf.*, Jun. 2007, pp. 1658–1664.

[9] M. Ordonez, J. E. Quaicoe, and M. T. Iqbal, "Advanced boundary control of inverters using the natural switching surface: Normalized geometrical derivation," *IEEE Trans. Power Electron.*, vol. 23, no. 6, pp. 2915–2930, Nov. 2008.

[10] J. Y. C. Chiu, K. K. S. Leung, and H. S. H. Chung, "High-order switching surface in boundary control of inverters," *IEEE Trans. Power Electron.*, vol. 22, no. 5, pp. 1753–1765, Sep. 2007.

[11] W. T. Yan, C. Ho, H. Chung, and K. Au, "Fixed-frequency boundary control of buck converter with second-order switching surface," *IEEE Trans. Power Electron.*, vol. 24, no. 9, pp. 2193–2201, Sep. 2009.

[12] K. K. S. Leung and H. S. H. Chung, "Derivation of a second-order switching surface in the boundary control of buck converters," *IEEE Power Electron. Lett.*, vol. 2, no. 2, pp. 63–67, Jun. 2004.

[13] K. K. S. Leung and H. S. H. Chung, "A comparative study of boundary control with first- and second-order switching surfaces for buck converters operating in DCM," *IEEE Trans. Power Electron.*, vol. 22, no. 4, pp. 1196–1209, Jul. 2007.

[14] T. Kerekes, R. Teodorescu, P. Rodriguez, G. Vazquez, and E. Aldabas, "A new high-efficiency single-phase transformerless PV inverter topology," *IEEE Trans. Ind. Electron.*, vol. 58, no. 1, pp. 184–191, Jan. 2011.

[15] T. Liang, R. M. O'Connell, and R. G. Hoft, "Inverter harmonic reduction using Walsh function harmonic elimination method," *IEEE Trans. Power Electron.*, vol. 12, no. 6, pp. 971–982, Nov. 1997.

[16] C. Qiao, K. M. Smedley, and F. Maddaleno, "A single-phase active power filter with one-cycle control under unipolar operation," *IEEE Trans. Circuits Syst. I, Regul. Papers*, vol. 51, no. 8, pp. 1623–1630, Aug. 2004.

[17] R. Gonzalez, J. Lopez, P. Sanchis, and L. Marroyo, "Transformerless inverter for single-phase photovoltaic systems," *IEEE Trans. Power Electron.*, vol. 22, no. 2, pp. 693–697, Mar. 2007.

[18] P. K. W. Chan, H. S.-H. Chung, and S. Y. Hui, "A generalized theory of boundary control for a single-phase multilevel inverter using second-order switching surface," *IEEE Trans. Power Electron.*, vol. 24, no. 10, pp. 2298–2313, Oct. 2009.

[19] C. Zhao *et al.*, "Design and implementation of GaN-based, 100 kHz, 102 W/in3 single-phase inverter," *IEEE J. Emerging Sel. Topics Power Electron.*, vol. 4, no. 3, pp. 824–840, Sep. 2016.

[20] A. Morsy and P. Enjeti, "Comparison of active power decoupling methods for high power density single phase inverters using wide band gap FETS for Google little box challenge," *IEEE J. Emerging Sel. Topics Power Electron.*, vol. 4, no. 3, pp. 790–798, Sep. 2016.

[21] *IEEE Recommended Practice and Requirements for Harmonic Control in Electric Power Systems*, IEEE Standard 519-2014, 2014.

[22] B. Crowhurst, E. F. El-Saadany, L. El Chaar, and L. A. Lamont, "Single-phase grid-tie inverter control using DQ transform for active and reactive load power compensation," in *Proc. IEEE Int. Conf. Power Energy*, Nov. 2010, pp. 489–494.

[23] H. Liu, "Control design of a single-phase dc/ac inverter for PV applications," *Master's theses*, Univ. Arkansas, Fayetteville, AR, USA, May 2016.

Mandip Pokharel (S'16) received the Bachelor's degree in electrical and electronics engineering from Kathmandu University, Dhulikhel, Nepal, in 2008, and the Master's degree in electrical power engineering jointly from the Norwegian University of Science and Technology, Trondheim, Norway, and Kathmandu University, under NORAD fellowship, in 2012. Currently, he is working toward the Ph.D. degree at the University of Manitoba, Winnipeg, MB, Canada.

Before joining the University of Manitoba, he worked as a Design and Project Engineer in various transmission line and substation based projects. His research interests include control system for power electronic applications, renewable energy, solar and wind emulators, real-time simulations, and power hardware in the loop simulations.

Nicolai Hildebrandt (S'13–M'14–S'18) received the Dipl.-Ing. degree in electrical engineering and information technologies from the Karlsruhe Institute of Technology (KIT), Karlsruhe, Germany, in 2013.

From 2006 to 2014, he was an Employee and Intern with the R&D Departments of Ringwald Mikroelektronik, Linde Material Handling, and KIT, all Germany, Bombardier Transportation and ABB Corporate Research, both Switzerland. From 2014 to 2017, he led industrial R&D projects at the Fraunhofer Institute for Solar Energy Systems ISE, Freiburg, Germany. In July 2017, he joined the Power Electronics Laboratory, Swiss Federal Institute of Technology, Lausanne, Switzerland, as a Doctoral Assistant. His research interests include high-power multilevel converters for medium-voltage applications, advanced control, and wide bandgap power devices.

Carl Ngai Man Ho (M'07–SM'12) received the B.Eng. and M.Eng. double degrees and the Ph.D. degree in electronic engineering from The City University of Hong Kong, Kowloon, Hong Kong, in 2002 and 2007, respectively.

From 2002 to 2003, he was a Research Assistant with the City University of Hong Kong. From 2003 to 2005, he was an Engineer with e.Energy Technology Ltd., Kowloon Tong, Hong Kong. In 2007, he joined ABB Switzerland Ltd., Baden, Zürich, Switzerland. He has been appointed as Scientist, Principal Scientist, Global Intellectual Property Coordinator, and R&D Principal Engineer. He has led a research project team with ABB to develop solar inverter technologies. In October 2014, he joined the University of Manitoba, Winnipeg, MB, Canada, as an Assistant Professor and a Canada Research Chair in Efficient Utilization of Electric Power. He established the Renewable-Energy Interface and Grid Automation Lab, University of Manitoba, to research on microgrid technologies, renewable energy interfaces, real-time digital simulation technologies, and demand side control methodologies.

Dr. Ho is currently an Associate Editor for the IEEE TRANSACTIONS ON POWER ELECTRONICS and the IEEE JOURNAL OF EMERGING AND SELECTED TOPICS IN POWER ELECTRONICS.

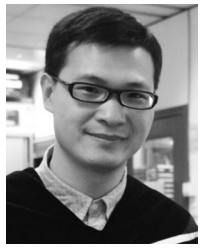

Yuanbin He (S'14–M'16) received the Ph.D. degree in electrical engineering from The City University of Hong Kong, Kowloon, Hong Kong, in 2017

He was a Research Assistant from April to August 2013 and a Postdoctoral Research Fellow from February to July 2017 with The City University of Hong Kong. From July 2011 to March 2013, he worked as an Associate Researcher with Nanjing FSP-Powerland Technology Inc., Nanjing, China, where he has been engaged in research and development of dc–dc and dc–ac converters. During February to June 2016, he was a Visiting Scholar with the University of Manitoba, Winnipeg, MB, Canada. Since May 2017, he has been with the Hangzhou Dianzi University, Hangzhou, China, where he is currently a Research Associate Professor in the Department of Electrical Engineering and Automation. His current research interests include renewable energy generation system, power quality, and smart grid.